Radiology

Opportunities in Interventional and Diagnostic Imaging by Using High-Performance Low-Field-Strength MRI

Adrienne E. Campbell-Washburn, PhD • Rajiv Ramasawmy, PhD • Matthew C. Restivo, PhD • Ipshita Bhattacharya, PhD • Burcu Basar, MSc • Daniel A. Herzka, PhD • Michael S. Hansen, PhD • Toby Rogers, BM BCh, PhD • W. Patricia Bandettini, MD • Delaney R. McGuirt, BSc • Christine Mancini, RT (R)MR • David Grodzki, PhD • Rainer Schneider, PhD • Waqas Majeed, PhD • Himanshu Bhat, PhD • Hui Xue, PhD • Joel Moss, MD, PhD • Ashkan A. Malayeri, MD • Elizabeth C. Jones, MD • Alan P. Koretsky, PhD • Peter Kellman, PhD • Marcus Y. Chen, MD • Robert J. Lederman, MD • Robert S. Balaban, PhD

From the Cardiovascular Branch, Division of Intramural Research, National Heart, Lung, and Blood Institute, National Institutes of Health, Bethesda, Md (A.E.C.W., R.R., M.C.R., I.B., B.B., D.A.H., M.S.H., T.R., W.P.B., D.R.M., C.M., M.Y.C., R.J.L.); Siemens Healthcare GmbH, Erlangen, Germany (D.G., R.S.); Siemens Medical Solutions Inc, Malvern Pa (W.M., H.B.); Systems Biology Center, Division of Intramural Research, National Heart, Lung, and Blood Institute, National Institutes of Health, 10 Center Dr, Building 10, Room 4C-1581, Bethesda, MD 20892-1458 (H.X., P.K., R.S.B.); Pulmonary Branch, Division of Intramural Research, National Heart, Lung, and Blood Institute, National Institutes of Health, Bethesda, MD (J.M.); Department of Radiology and Imaging Sciences, Clinical Center, National Institutes of Health, Bethesda, Md (A.A.M., E.C.J.); and Laboratory of Functional and Molecular Imaging, Division of Intramural Research, National Institute of Neurologic Disorders and Stroke, National Institutes of Health, Bethesda, Md (A.P.K.). Received February 26, 2019; revision requested April 15; revision received August 6; accepted August 15. **Address correspondence to** R.S.B. (e-mail: *rsb@nih.gov*).

Study supported by the Division of Intramural Research, National Heart, Lung and Blood Institute, National Institutes of Health (ZO1-HL006213, ZO1-HL006214, ZO1-HL005062, ZO1-HL006039).

Conflicts of interest are listed at the end of this article.

See also the editorial by Grist in this issue.

Radiology 2019; 293:384–393 • https://doi.org/10.1148/radiol.2019190452 • Content codes: MR PH

Background: Commercial low-field-strength MRI systems are generally not equipped with state-of-the-art MRI hardware, and are not suitable for demanding imaging techniques. An MRI system was developed that combines low field strength (0.55 T) with high-performance imaging technology.

Purpose: To evaluate applications of a high-performance low-field-strength MRI system, specifically MRI-guided cardiovascular catheterizations with metallic devices, diagnostic imaging in high-susceptibility regions, and efficient image acquisition strategies.

Materials and Methods: A commercial 1.5-T MRI system was modified to operate at 0.55 T while maintaining high-performance hardware, shielded gradients (45 mT/m; 200 T/m/sec), and advanced imaging methods. MRI was performed between January 2018 and April 2019. T1, T2, and T2* were measured at 0.55 T; relaxivity of exogenous contrast agents was measured; and clinical applications advantageous at low field were evaluated.

Results: There were 83 0.55-T MRI examinations performed in study participants (45 women; mean age, 34 years ± 13). On average, T1 was 32% shorter, T2 was 26% longer, and T2* was 40% longer at 0.55 T compared with 1.5 T. Nine metallic interventional devices were found to be intrinsically safe at 0.55 T (<1°C heating) and MRI-guided right heart catheterization was performed in seven study participants with commercial metallic guidewires. Compared with 1.5 T, reduced image distortion was shown in lungs, upper airway, cranial sinuses, and intestines because of improved field homogeneity. Oxygen inhalation generated lung signal enhancement of 19% ± 11 (standard deviation) at 0.55 T compared with 7.6% ± 6.3 at 1.5 T ($P = .02$; five participants) because of the increased T1 relaxivity of oxygen (4.7e−4 $mmHg^{-1}sec^{-1}$). Efficient spiral image acquisitions were amenable to low field strength and generated increased signal-to-noise ratio compared with Cartesian acquisitions ($P < .02$). Representative imaging of the brain, spine, abdomen, and heart generated good image quality with this system.

Conclusion: This initial study suggests that high-performance low-field-strength MRI offers advantages for MRI-guided catheterizations with metal devices, MRI in high-susceptibility regions, and efficient imaging.

Online supplemental material is available for this article.

In North America most clinical MRI is performed at 1.5 T or 3.0 T, and some research applications have moved to 7.0 T. High field is motivated by higher polarization, promising increased signal-to-noise ratio (SNR), and resolution. However, this causes image distortion, constrained imaging efficiency, increased specific absorption rate, and higher cost. For some applications, low field strength may offer intrinsic advantages (1,2). At low field strength, short T1 and long T2* allow more efficient pulse sequence design; imaging near air-tissue interfaces is improved by virtue of reduced susceptibility gradients; and specific absorption rate is reduced, which can diminish heating of conductive devices and implants, and can eliminate pulse sequence parameter constraints (3). Commercial lower field systems have been largely overlooked as hardware and software have improved over the last 2 decades, and therefore are not well-suited for technically demanding imaging. We developed and evaluated a custom 0.55-T MRI system equipped with contemporary

Abbreviation

SNR = signal-to-noise ratio

Summary

Low-field MRI combined with contemporary high-performance MRI hardware and advanced image acquisition and reconstruction strategies has advantages for some technically demanding applications including MRI-guided interventions, imaging anatomy near air-tissue interfaces, and efficient image acquisition methods.

Key Results

- We performed 83 MRI examinations in study participants (83 participants; 45 women; mean age, 34 years ± 13 [standard deviation]) with a custom 0.55-T MRI system that combines low field strength with contemporary hardware and imaging methods.
- MRI-guided cardiovascular catheterizations were performed in seven study participants with commercially available metallic guidewires that generate negligible heating during real-time MRI at 0.55 T.
- High-performance low-field-strength MRI reduced image distortion in high-susceptibility regions, including the lung, and oxygen was determined to have high T1 relaxivity ($4.7e{-}4$ $mmHg^{-1}sec^{-1}$) at 0.55 T, allowing greater signal intensity enhancement at inhalation of 100% oxygen, compared with 1.5 T ($P = .02$).

magnet, gradient, and radiofrequency systems for advanced imaging applications.

We characterized in vivo tissue relaxation parameters and exogenous contrast agent performance at 0.55 T. We then demonstrated applications that may be well suited to a high-performance low-field-strength MRI platform. Finally, we tested early feasibility of routine MRI with this system configuration.

We chose three technically demanding applications for this initial investigation. First, we hypothesized that high-performance low-field-strength MRI could offer reduced device heating with sufficient real-time cardiac imaging performance to accomplish catheter navigation in study participants. Low field may obviate the radiofrequency-induced heating that has hampered the clinical adoption of MRI cardiovascular catheterization (4,5). Second, by leveraging reduced absolute susceptibility, which is linear with field strength, low field strength can improve imaging near air-tissue interfaces. We predict that our contemporary 0.55-T system will improve image quality in anatomy near the cranial sinuses, lungs, airways, and intestines, which can be irrevocably distorted at higher fields. Third, we propose that SNR-efficient imaging that leverages short T1 and prolonged T2* at low field strength, such as echo-planar imaging and spiral readouts, is amenable to lower fields.

The purpose of this study was to evaluate applications of a high-performance low-field-strength MRI system, specifically MRI-guided cardiovascular interventions, diagnostic imaging in high-susceptibility regions, and efficient imaging schemes.

Materials and Methods

Our institutional review board approved this study and written informed consent was obtained from all participants. Employees of Siemens Healthcare assisted with system modification. The first and senior authors controlled the data. Between January 2018 and April 2019, we performed 83 research MRI examinations in 83 participants (45 female participants; mean age, 34 years ± 13 [standard deviation]). We performed 68 examinations in healthy participants and 15 examinations in participants with disease. Participants underwent technical development imaging ($n = 38$; 23 female participants; mean age, 34 years ± 14), parametric mapping ($n = 38$; 17 female participants; mean age, 31 years ± 11), or MRI-guided catheterization procedures ($n = 7$; five female participants; mean age, 49 years ± 17).

MRI System

We modified a commercial MRI system (1.5-T Magnetom Aera; Siemens Healthcare, Erlangen, Germany) to operate at 0.55 T and retain gradient performance (maximum gradient amplitude, 45 mT/m; maximum slew rate, 200 T/m/sec). Phased-array receiver coils including an 18-channel spine array, six-channel body arrays, and a 16-channel head array were retuned to 23.6 MHz and used for imaging. We performed comparison studies at 1.5 T (Magnetom Aera, Siemens Healthcare).

Heating Experiments

Standard procedure American Society for Testing and Materials, or ASTM, 2182F (6) (ASTM International, *https://www.astm.org/Standards/F2182.htm*) was used to assess the heating of conductive devices and implants at 0.55 T with fiberoptic temperature probes (OpSens Solutions, Quebec, Canada). Sixteen commercial nitinol guidewires and stainless-steel braided catheters considered to be unsafe at 1.5 T were evaluated as candidates for MRI-guided catheterization at conditions known to generate maximal heating (7) (Table E1 [online]). For the purpose of clinical catheterization, we defined a safety margin of less than 1°C of heating at the device tip during 2 minutes of continuous, high-specific-absorption-rate, real-time imaging (flip angle, 65°; radiofrequency pulse length, 600 μsec; repetition time msec, 2.5). To assess cardiovascular implantable electronic device safety at 0.55 T, heating at the tip of 50-cm pacemaker leads (Vitalio Pacemaker; Boston Scientific Corporation, Marlborough, Mass) was evaluated according to ASTM 2182F.

Patient Catheterization

Seven study participants (mean age, 49 years ± 16; five women) underwent clinically indicated right heart catheterization guided by real-time MRI fluoroscopy. Transfemoral access was attained in the adjoining radiography catheterization laboratory, and a polymer balloon wedge end-hole catheter (t-tip, dual-lumen including inflation port, 7 F × 110 cm, 0.038-inch lumen; Swan-Ganz Flow-Directed Monitoring Catheter Model T111F7, Edwards Lifesciences, Irvine, Calif) was guided to the inferior vena cava, superior vena cava, right atrium, right ventricle, main pulmonary artery, and branched pulmonary arteries into a wedge position with MRI guidance for invasive pressure measurements. Catheter navigation used multiplanar real-time balanced steady-state free precession imaging (repetition time msec/echo time msec, 4/2; flip angle, 45°; field of view, 400 mm; section thickness, 8–24 mm, 160

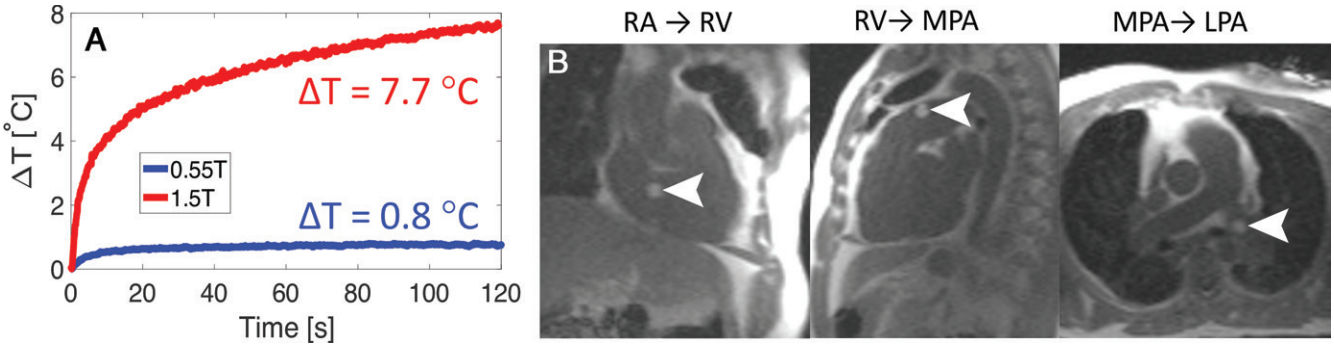

Figure 1: *A*, Reduced heating during real-time MRI is illustrated for a metallic commercial guidewire (180 cm × 0.035 inches with angled tip; Glidewire, Terumo, Tokyo, Japan). *B*, A balloon filled with gadolinium chelate is shown (arrowheads) during navigation of a metallic guidewire for MRI-guided right heart catheterization in a 64-year-old woman. Standard balanced steady-state free precession imaging with a partial saturation preparation was used for imaging at 0.55 T (repetition time msec/echo time msec, 4/2; flip angle, 45°; field of view, 400 mm; section thickness, 8–24 mm; 160 × 144 matrix; acceleration factor of two; partial saturation prepulse [8] flip angle, 60°). ΔT = change in temperature following 2 minutes of continuous real-time balanced steady-state free precession imaging, LPA = left pulmonary artery, MPA = main pulmonary artery, RA = right atrium, RV = right ventricle.

× 144 matrix; acceleration factor of two; and 3.4 frames per second). A nonselective magnetization preparation pulse (8) (flip angle, 60°) was applied before each image to view the balloon catheter tip filled with dilute gadolinium chelate (gadobutrol, 0.5% dilution from stock). A conductive metallic guidewire (180 cm × 0.035 inches; GR3525 Glidewire Micro J-tip, Terumo, Tokyo, Japan) was used as an adjunct.

Imaging Near Air-Tissue Interfaces

To evaluate imaging near air-tissue interfaces, T2-weighted fast s-echo images of the lung were acquired in one healthy female participant (age, 26 years) and in one woman with lymphangioleiomyomatosis (9) (age, 54 years) at both 0.55 T and 1.5 T. Inhalation of 100% oxygen at 15 L/min through a nonrebreather mask was used for signal intensity enhancement in the lung (10–12) with T1-weighted ultra-short echo-time imaging. We measured changes in signal intensity, lung T1, and arterial blood T1 between inhalation of room air and oxygen in five matched participants (three women; mean age, 35 years ± 14) at 0.55 T and 1.5 T. In addition, we performed imaging of the upper airway for real-time sleep and speech imaging (13) applying a golden angle spiral acquisition with a 9.4-msec readout duration at 0.55 T and 1.5 T for image quality comparison (two male participants, ages 24 and 28 years). Real-time speech images were reconstructed with a compressed sensing method that constrains temporal finite difference (temporal resolution = 1, repetition time = 11 msec) (14,15). We assessed single-shot echo-planar imaging distortion of diffusion-weighted imaging in high-susceptibility regions near the cranial sinus and near the intestines in matched participants at 0.55 T and 1.5 T (two male participants, ages 30 and 32 years).

Imaging Efficiency

Efficient data sampling strategies are well suited to low field strength because prolonged T2* allows for longer signal readouts and shorter T1 permits shorter repetition time. We implemented SNR-efficient spiral-out balanced steady-state free precession (16) and spiral-out spin-echo (17) acquisitions with prolonged data sampling readouts (balanced steady-state free precession readout, 6 msec; spin-echo readout, 21 msec) to exploit these relaxation properties. We did not use off-resonance correction because blurring is minimal due to field homogeneity. K-space trajectory correction used the gradient system impulse response function measured for the system (18). The SNR of spiral-out acquisitions at 0.55 T, Cartesian acquisitions at 0.55 T, and Cartesian acquisitions at 1.5 T were compared in healthy participants for blood and myocardium (balanced steady-state free precession sequence, seven participants [six women]; mean age, 24 years ± 4), and white matter and gray matter (spin echo sequence, five participants [three women]; mean age, 35 years ± 17). Importantly, we fixed total image acquisition time between comparator protocols and only modified sampling efficiency, defined as time sampling data per total acquisition time, to increase SNR (19). We calculated SNR by the method of pseudoreplicas (20).

Image Contrast

We measured T1, T2, and T2* in vivo in the white matter, gray matter, myocardium, arterial blood pool, liver, lung, kidney cortex, and fat (39 participants; 17 women; mean age, 31 years ± 12), and compared measurements to values for 1.5 T in the literature (imaging parameters and 1.5-T references are provided in Appendix E1 Materials section [online]).

T1 and T2 relaxivity (r1 and r2) of clinical gadolinium-based contrast agents, oxygen, and larger molecular-weight contrast agents ferumoxytol, gadofosveset, and gadolinium dendrimers were calculated. Contrast agents were diluted in phosphate-buffered saline and relaxivity was measured at room temperature at 0.55 T and 1.5 T (Table E2 [online]).

Routine Imaging

We performed routine MRI sequences for imaging brain, abdomen, spine, and heart by using this system configuration for both healthy participants and patients with known pathologic abnormalities (seven participants [five women]; mean age, 35

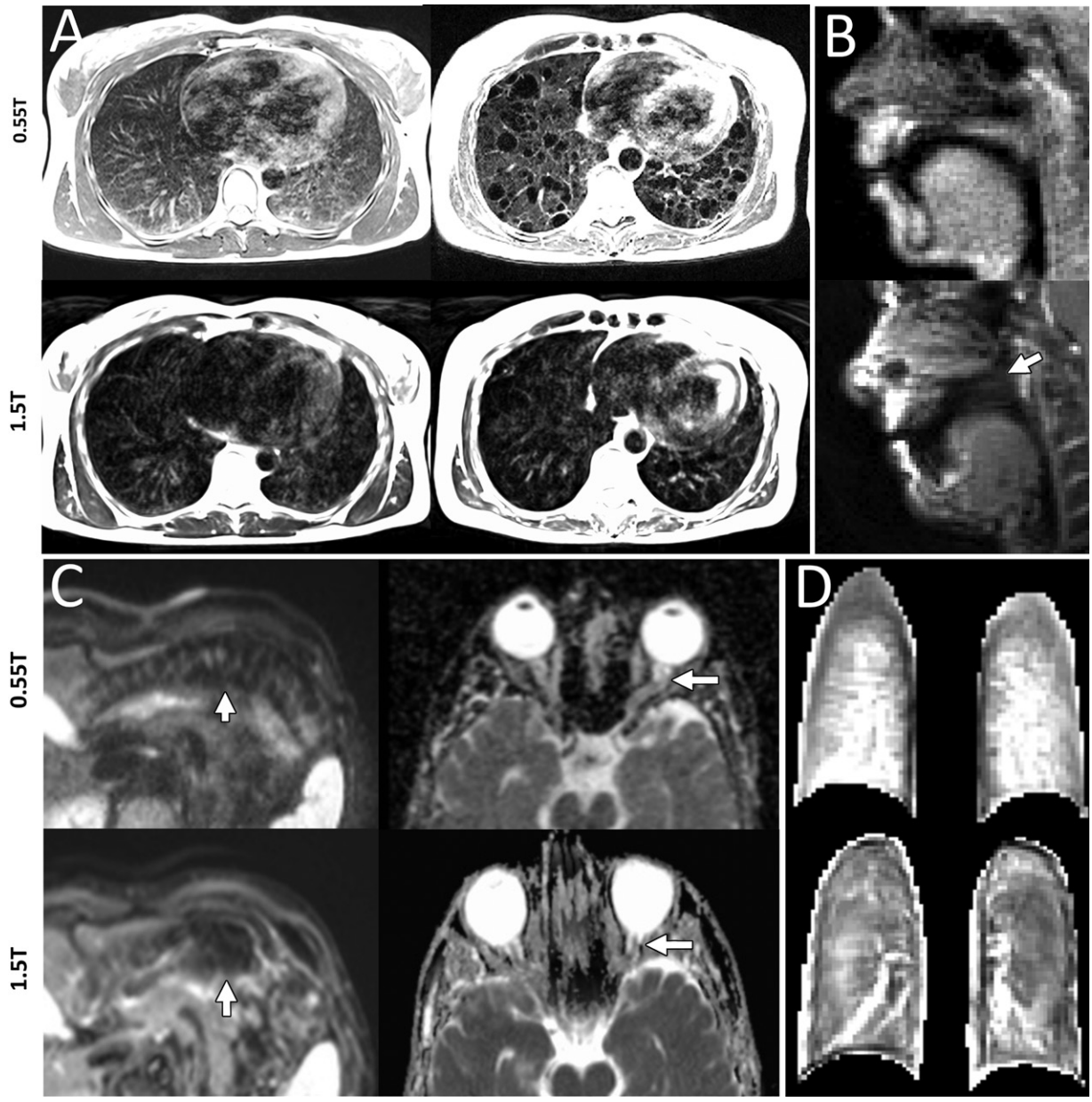

Figure 2: *A*, Lungs show increased signal intensity at 0.55 T compared with 1.5 T because of improved field homogeneity demonstrated in a healthy 26-year-old woman and a 54-year-old woman with lymphangioleiomyomatosis (T2-weighted fast spin echo; repetition time msec/echo time msec, 4403/47; field of view, 270 × 360 mm; 480 × 640; 32 sections; section thickness, 6 mm; bandwidth, 260 Hz per pixel; respiratory triggered). ***B***, Reduced image distortion around air-tissue interfaces is shown in two men (ages 24 years and 28 years) for real-time speech imaging, wherein the velum is not visible at 1.5 T because of off-resonance blurring (arrow; pseudo–golden angle spiral gradient echo; section thickness, 10 cm; field of view, 280 mm × 280 mm; spatial resolution, 2.2 × 2.2 mm; 11.3/0.86; sampling duration, 9.4 msec; acceleration factor of six). ***C***, Single-shot echo-planar diffusion-weighted imaging near the bowel in a 32-year-old man shows improved boundary delineation at 0.55 T (left), and apparent diffusion coefficient map near the sinuses in a 30-year-old man shows improved delineation of the optic nerve at 0.55 T (right) (abdomen imaging at 0.55 T [left]: field of view, 313 × 380 mm; 132 × 160 matrix; ***b*** value, 50; 30 sections; section thickness, 6 mm; 2500/91; receiver bandwidth, 1200 Hz per pixel; acceleration factor of four; echo train length, 57; acquisition time, 2:19 minutes; abdomen imaging at 1.5 T [left]: field of view, 274 × 340 mm; 108 × 134 matrix; ***b*** value, 0; 31 sections; section thickness, 6 mm; 5700/59; receiver bandwidth, 2300 Hz per pixel; acceleration factor of two; echo train length, 53; acquisition time, 3:32 minutes; brain imaging at 0.55 T [right]: field of view, 229 × 229 mm; 176 × 176 matrix; *b* values, 0 and 1000; 20 sections; section thickness, 5 mm; 4000/80; receiver bandwidth, 860 Hz per pixel; acceleration factor of two; echo train length, 53; acquisition time, 2:38 minutes; and brain imaging at 1.5 T [right]: field of view, 229 × 229 mm; 176 × 176 matrix; ***b*** values, 0 and 1000; three averages; 21 sections; section thickness, 5 mm; 6300/89; receiver bandwidth, 1130 Hz per pixel; acceleration factor of two; echo train length, 71; acquisition time, 1:36 minutes). ***D***, T1-weighted ultrashort echo time lung images during inhalation of 100% oxygen in a 19-year-old man show higher signal intensity, normalized to skeletal muscle, at 0.55 T (three-dimensional stack of spirals; gradient echo; 8.54/0.15 [at 0.55 T] and 6.21/0.17 [at 1.5 T]; flip angle, 20°; section thickness, 10 mm; field of view, 450 mm; 128 × 128 matrix; 16-shot spiral design; readout length, 7 msec [at 0.55 T] and 5 msec [at 1.5 T]).

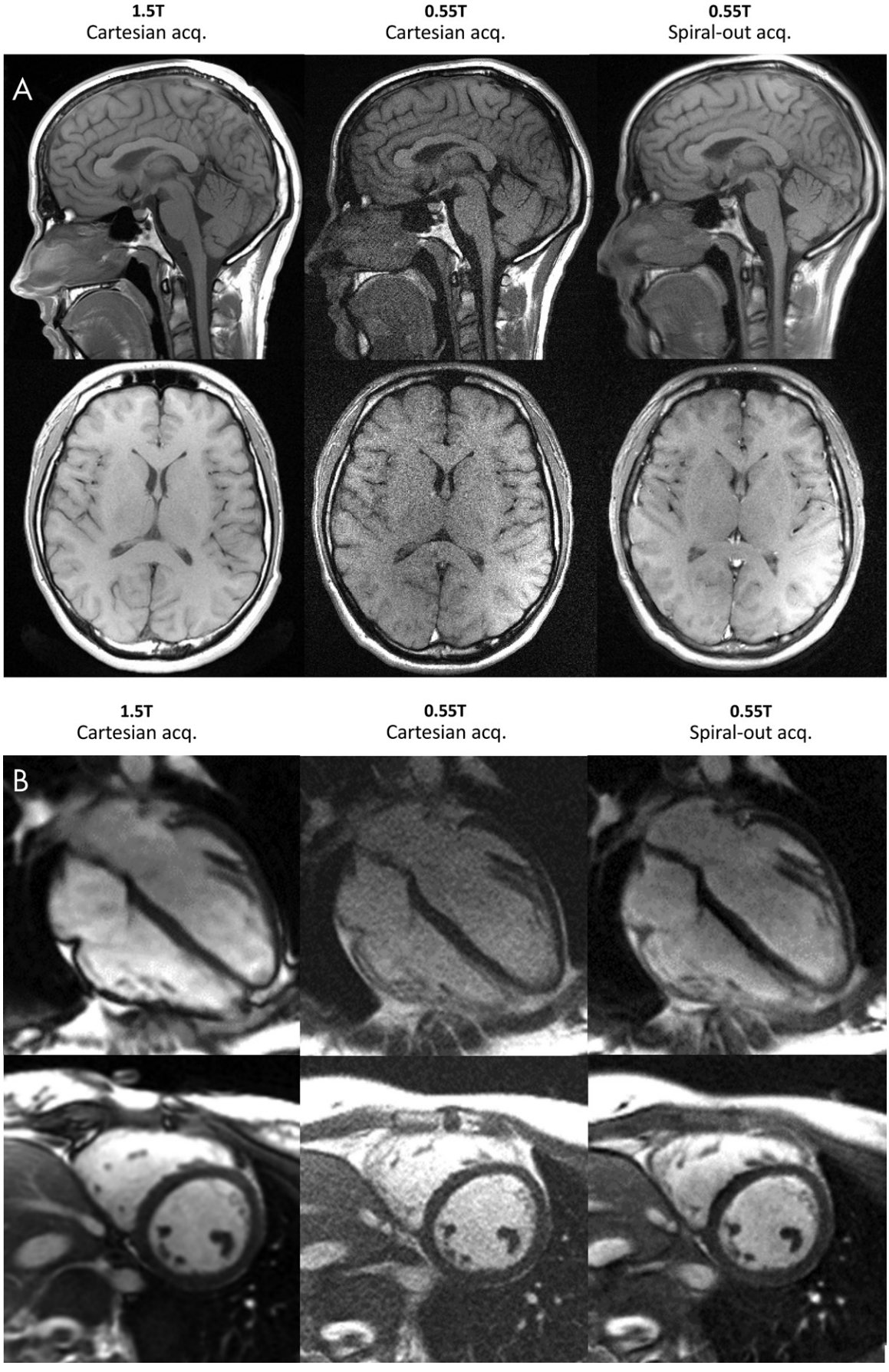
1.5T
Cartesian acq.
0.55T
Cartesian acq.
0.55T
Spiral-out acq.
A
1.5T
Cartesian acq.
0.55T
Cartesian acq.
0.55T
Spiral-out acq.
B

years ± 16). This is not intended to be an exhaustive evaluation of imaging methods or to provide a quantitative image quality comparison but rather to provide illustrative examples of image quality.

Statistical Analysis

Small sample sizes were used in this exploratory study. Values are reported as means ± standard deviation where applicable. We used paired Student *t* tests to compare lung signal intensity enhancement, change in T1 of arterial blood and change in T1 of lung tissue following oxygen inhalation at 0.55 T and 1.5 T, and to compare SNR of the blood, myocardium, gray matter, and white matter between two MRI sampling strategies. *P* values less than .05 were considered to indicate statistical significance. Bonferroni correction was applied when multiple comparisons were calculated from the same data set.

Results

Patient Catheterization

Radiofrequency-induced heating increases quadratically with field strength, indicating a theoretical 7.5-fold difference in heating between 0.55 T and 1.5 T. Among the 16 commercially available conductive catheterization devices that underwent heating measurements, we identified nine devices that produced less than 1°C of heating during 2 minutes of continuous imaging (Fig 1, *A*, Table E1 [online]). As expected, fully

Table 1: Tissue Relaxation Parameters at 0.55 T versus Reference 1.5-T Values

Tissue	T1 (msec)	T2 (msec)	T2* (msec)	T2*-to-T2 Ratio (%)
White matter				
0.55 T	493 ± 33	89 ± 9	72 ± 12	81
1.5 T	608–884	54–96	48–60	72
Gray matter				
0.55 T	717 ± 82	112 ± 7	86 ± 9	77
1.5 T	1002–1304	93–109	67–79	72
Myocardium				
0.55 T	701 ± 24	58 ± 6	47 ± 4	80
1.5 T	950–1030	40–58	30–37	68
Arterial blood				
0.55 T	1122 ± 85	263 ± 27	...	...
1.5 T	1441–1898	254–290	...	...
Liver				
0.55 T	339 ± 31	66 ± 6	43 ± 4	65
1.5 T	576–586	46–55	26–33	59
Lung				
0.55 T	971 ± 62	61 ± 11	10 ± 2	17
1.5 T	1171–1333	41	1–2	5
Kidney cortex				
0.55 T	651 ± 48	101 ± 7	82 ± 17	82
1.5 T	690–966	55–87	49–51	70
Fat				
0.55 T	187 ± 10	93 ± 16	...	...
1.5 T	288–343	53–84	...	...

Note.—The 0.55-T values are means ± standard deviation; the 1.5-T values are ranges. Imaging sequence parameters and 1.5T reference list are provided in Appendix E1 Materials section (online). T2*-to-T2 ratio was calculated from mean values. For 0.55 T, participants were as follows: white/gray matter, nine participants (mean age, 31 years ± 12; six women); myocardium/blood/lung, 22 participants (mean age, 35 years ± 12; six women); and liver/kidney/fat, seven participants (mean age, 23 years ± 4; five women).

Figure 3: Signal-to-noise ratio–efficient spiral imaging applied for, *A*, T1-weighted neuroimaging in a 23-year-old woman (axial sections) and a 28-year-old woman (sagittal sections), and, *B*, balanced steady-state free precession cardiac imaging demonstrated in a 23-year-old woman. Total acquisition time was fixed, but sampling efficiency was increased with spiral acquisitions. Good image quality and signal-to-noise ratio improvements at 0.55T are observed with the spiral sampling scheme. Images were acquired with Cartesian sampling at 1.5 T and 0.55 T, and spiral-out at 0.55 T (1.5-T Cartesian spin echo: field of view [FOV], 216 × 230 mm; 240 × 320 matrix; section thickness, 5 mm; repetition time msec/echo time msec, 550/8.9; receiver bandwidth, 150 Hz per pixel; acquisition time, 1:33 minutes; 0.55-T Cartesian spin echo: FOV, 215 × 230 mm; 240 × 320 matrix; section thickness, 5 mm; 450/9.3; receiver bandwidth, 110 Hz per pixel; acquisition time, 2:20 minutes; 0.55-T spiral-out spin echo: FOV, 230 × 230 mm; 320 × 320 matrix; 500/15; section thickness, 5 mm; 24-shot spiral design; readout length, 21 msec; 1.5-T Cartesian balanced steady-state free precession: FOV, 270 × 360 mm; 140 × 256 matrix; section thickness, 8 mm; 2.79/1.2; receiver bandwidth, 1085 Hz per pixel; acquisition time, 9 seconds; 0.55-T Cartesian balanced steady-state free precession: FOV, 270 × 360 mm; 192 × 256 matrix; section thickness, 8 mm; 4.1/1.67; receiver bandwidth, 350 Hz per pixel; acquisition time, 9 seconds; 0.55-T spiral-out balanced steady-state free precession: FOV, 360 × 360 mm; 256 × 256 matrix; 8/0.86; section thickness, 8 mm; 66-shot spiral design; readout length, 6 msec; zeroth and first moment balancing of gradients).

Table 2: Relaxivity of Clinical and Experimental Contrast Agents at 0.55 T and 1.5 T

	r1		r2	
Contrast Agent	0.55 T	1.5 T	0.55 T	1.5 T
Gadobutrol ($mM^{-1}sec^{-1}$)	5.2	5.5	7.0	6.8
Gadoterate meglumine ($mM^{-1}sec^{-1}$)	3.4	4.6	6.1	5.7
Gadopentetate dimeglumine ($mM^{-1}sec^{-1}$)	3.8	3.3	5.9	3.9
Gadofosveset ($mM^{-1}sec^{-1}$)	7.8	7.3	8.4	8.6
Gadofosveset with 0.2-mM human serum albumin ($mM^{-1}sec^{-1}$)	11.7	9.5	13.2	14.5
Ferumoxytol ($mM^{-1}sec^{-1}$)	35.7	18.0	97.3	87.0
Gd-dendrimers ($mM^{-1}sec^{-1}$)	64.0	NA*	93.6	…
Oxygen ($mmHg^{-1}sec^{-1}$)	4.7e−4	3.1e−4	3.3e−4	…

Note.—Contrast agent dilutions and imaging parameters are provided in Appendix E1 Materials section (online). NA = not applicable.
* 12 $mM^{-1}sec^{-1}$ at 3 T.

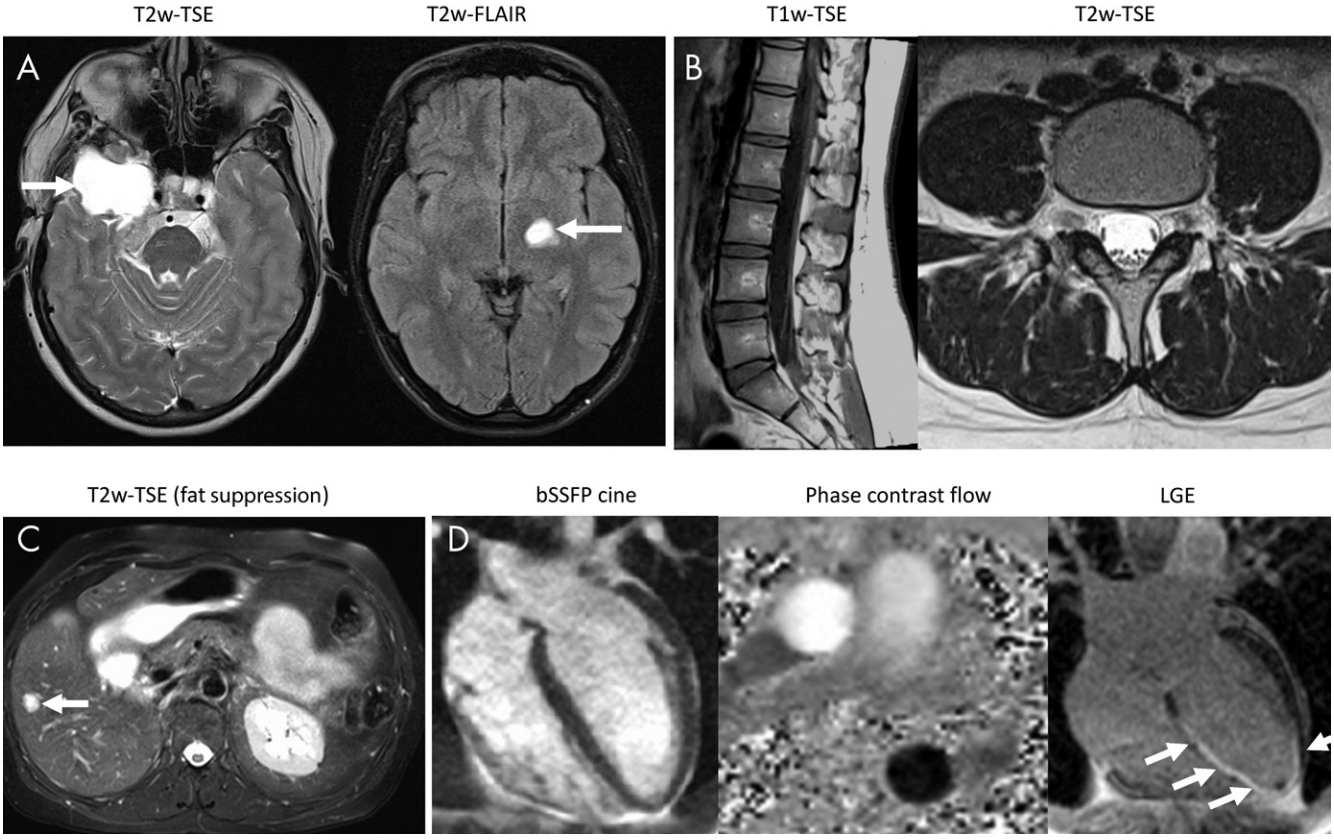

Figure 4: Images show common pulse sequences that were applied to study participants to illustrate routine image quality with a 0.55-T system configuration. *A*, T2-weighted (T2w)–turbo spin echo (TSE; left side) in a 42-year-old woman with meningioma and postcontrast T2w fluid-attenuated inversion recovery (FLAIR; right side) images in 22-year-old woman with a low-grade tumor (T2w-FSE: field of view [FOV], 229 × 229 mm; 176 × 176 matrix; eight signal averages; 20 sections; section thickness, 5 mm; repetition time msec/echo time msec, 4000/80; receiver bandwidth, 860 Hz per pixel; acceleration factor of two; echo train length, 65; acquisition time, 2:38 minutes; T2-FLAIR: FOV, 201 × 230 mm; 210 × 320 matrix; two averages; 20 sections; section thickness, 5 mm; 8000/95; inversion time, 2371 msec; receiver bandwidth, 120 Hz per pixel; echo train length, 15; acquisition time, 3:36 minutes). *B*, T1-weighted (T1w) and T2w-TSE images (left and right side, respectively) of the spine in a healthy 24-year-old woman (T1w-TSE: FOV, 260 × 260 mm; 240 × 320 matrix; five averages; 15 sections; section thickness, 4 mm; 396/13; receiver bandwidth, 110 Hz per pixel; acceleration factor of two; echo train length, 3; acquisition time, 5:16 minutes; T2w-TSE: FOV, 200 × 200 mm; 256 × 320 matrix; five averages; 15 sections; section thickness, 4 mm; 3200/89; receiver bandwidth, 120 Hz per pixel; echo train length, 15; acquisition time, 5:32 minutes). *C*, Successful fat suppression with T2w-TSE in the abdomen of a 64-year-old woman with a hepatic lesion (FOV, 308 × 380 mm; 231 × 320 matrix; four averages; 30 sections; section thickness, 6 mm; 4886/47; receiver bandwidth, 260 Hz per pixel; echo train length, 7; spectral selective fat suppression; acquisition time, 15:15 minutes). *D*, Cardiac balanced steady-state free precession cine (bSSFP cine) in a heathy 19-year-old man (left side), phase contrast flow measurement in a healthy 43-year-old woman (middle), and late gadolinium-chelate enhancement (LGE) images in a 42-year-old man with chronic myocardial infarction (right side) (bSSFP cine: FOV, 350 × 380 mm; 192 × 256 matrix; one signal average; section thickness, 8 mm; flip angle, 78°; 4.1/1.67; receiver bandwidth, 350 Hz per pixel; acceleration factor of two; breath-hold length, 9 seconds; phase contrast flow: FOV, 270 × 360 mm; 144 × 192 matrix; three averages; section thickness, 6 mm; flip angle, 25°; 7.6/3.71; receiver bandwidth, 200 Hz per pixel; acquisition time, 1:37 minutes; LGE: gradient echo; FOV, 300 × 400 mm; 144 × 256 matrix; one average; section thickness, 8 mm; flip angle, 25°; 8.3/3.16; receiver bandwidth, 140 Hz per pixel; breath-hold length, 12 seconds).

insulated devices and devices with shorter conductive length generated less heat than devices with exposed metal components. The pacemaker lead heated 0.5°C during 1 minute of continuous imaging at 0.55 T. These findings indicate the improved safety of cardiovascular implantable electronic devices and interventional devices at 0.55 T.

Clinical MRI-guided right heart catheterization at 0.55 T was successful in all seven study participants with an insulated nitinol guidewire and standard real-time imaging without modified sequence parameters (Fig 1, *B*). There was no evidence of heating caused by the guidewire and there were no adverse events in this small patient cohort. The guidewire provided interactive catheter stiffness and steerability for procedural navigation.

Imaging Near Air-Tissue Interfaces

We showed imaging in high-susceptibility regions near air-tissue interfaces by using four representative comparisons between 0.55 T and 1.5 T. First, imaging of cystic disease in the lung showed improved delineation of cysts at 0.55 T (Fig 2, *A*). Second, we demonstrate reduced off-resonance spiral blurring (21) in the upper airway during real-time speech imaging (Fig 2, *B*, Movie 1 [online]). Third, single-shot echo-planar diffusion-weighted imaging near the bowel showed reduced signal distortion caused by field inhomogeneity, and diffusion-weighted imaging near the cranial sinuses showed clear delineation of the optic nerve at 0.55 T, which indicated that the important fields of MRI fiber tractography and stroke characterization in the brain can be applied in these high-susceptibility brain regions (Fig 2, *C*).

We used oxygen inhalation for signal enhancement in T1-weighted images of lungs (Fig 2, *D*). Measured oxygen T1 relaxivity was greater at 0.55 T (r1, 4.7e–4 mm $Hg^{-1}sec^{-1}$) compared with 1.5 T (r1, 3.1e–4 mm $Hg^{-1}sec^{-1}$). As a result, the increase in signal intensity between images acquired at room air inhalation and oxygen inhalation was 19% ± 11 at 0.55 T versus 8% ± 6 at 1.5 T (five healthy participants, 10 sections; P = .02). Lung T1 shortened from 1003 msec ± 102 at inhalation of room air to 930 msec ± 50 at oxygen inhalation (change in T1, 11% ± 3) and arterial blood T1 shortened from 1135 msec ± 119 to 1045 msec ± 99 (change in T1, 14% ± 3). Change in T1 in the arterial blood was significantly greater at 0.55 T than at 1.5 T and approached significance in the lung (arterial blood at 1.5 T: T1 during room air inhalation, 1554 msec ± 104; T1 at oxygen inhalation, 1394 msec ± 107; change in T1, 10% ± 2; P = .007; lung at 1.5 T: T1 during room air inhalation, 1240 msec ± 85; T1 during oxygen inhalation, 1152 msec ± 91; change in T1, 7% ± 3; P = .08).

Imaging Efficiency

Spiral-out balanced steady-state free precession had a sampling efficiency of 70% compared with only 45% for Cartesian acquisitions. Similarly, spiral spin echo had an increased efficiency of 32% versus 15%. Figure 3 and Movie 2 (online) show the resulting image quality. As expected, SNR in all tissues significantly improved by using SNR-efficient spiral acquisitions (blood: SNR Cartesian acquisition, 15 ± 3; SNR spiral spin echo, 28 ± 8; P = .01; myocardium: SNR Cartesian acquisition, 6 ± 1, SNR spiral spin echo, 10 ± 3; P = .02; white matter: SNR Cartesian acquisition, 19 ± 3; SNR spiral spin echo, 38 ± 7; P = .003; gray matter: SNR Cartesian acquisition, 17 ± 3; SNR spiral spin echo, 33 ± 7; P = .009). By using these prototype spiral sequences, the average SNR recovered to 57% of that measured at 1.5 T applying comparable protocols (blood: SNR at 1.5 T, 63 ± 8; myocardium: SNR at 1.5 T, 17 ± 1; white matter: SNR at 1.5 T, 56 ± 11; gray matter: SNR at 1.5 T, 59 ± 10), indicating the potential of these techniques at low field.

Image Contrast

Table 1 compares relaxation parameters for a variety of tissues in vivo at 0.55 T to literature values for 1.5 T. The relative difference in relaxation parameters was not uniform across tissues. On average, T1 was 32% shorter at 0.55 T; T2 was 26% longer; and T2* was substantially longer by 40%, and 350% longer in the lung. The ratio of T2*-to-T2 was increased at low field strength where T2* approaches T2, especially in the thorax because of susceptibility of the torso.

As expected, T1 and T2 relaxivity of clinical small-molecular-weight gadolinium-based contrast agents were similar between 0.55 T and 1.5 T (Table 2) (22). We found that larger molecular complexes had increased T1 relaxivity at 0.55 T because of their correlation times, including ferumoxytol (23,24), gadofosveset bound to albumin (25), gadolinium dendrimers (26,27), and oxygen (range, 23%–98% increase compared with 1.5 T or 3.0 T). This indicates that lower doses may be feasible for angiographic imaging with intravascular contrast agents (eg, ferumoxytol and gadofosveset).

Routine Imaging

Figure 4 demonstrates application of the high-performance low-field-strength MRI for routine imaging of the brain, abdomen, spine, and heart in healthy participants and participants with known pathologic abnormalities. We observed good image quality, even for demanding applications such as diffusion-tensor imaging and cardiac MRI, with this high-performance 0.55-T system.

Discussion

Our work evaluated an MRI system that combines low magnetic field strength (0.55 T) with high-performance imaging hardware and contemporary imaging techniques applied for demanding imaging applications. Radiofrequency-induced heating was reduced at 0.55 T and nine of 16 endovascular devices were free from heating (<1°C during 2 minutes of real-time MRI), and seven study participants underwent MRI-guided diagnostic cardiovascular catheterization with commercial metallic devices. The reduced susceptibility of the high-performance 0.55-T MRI system was exploited for reduced distortion in lung imaging, real-time speech imaging, and diffusion imaging near air-tissue interfaces compared with 1.5 T. Large-molecular-weight contrast agents and oxygen demonstrated increased T1 relaxivity compared with 1.5 T (range, 23%–98% increase), and a significant increase in oxygen-enhanced lung signal intensity (P = .02) was observed. On average, in vivo T1 was 32% shorter, T2 was

26% longer, and T2* was 40% longer than at 1.5 T. Spiral-out acquisitions, which exploit the prolonged T2* for imaging efficiency, generated good image quality and significant increases in signal-to-noise ratio (SNR) for neuroimaging and cardiac imaging (range, 86%–100% increase in SNR). Standard pulse sequences evaluated for routine imaging with the high-performance 0.55-T system configuration provided reasonable image quality by contemporary standards.

Early in the development of clinical MRI there were system imperfections that limited the attainable image quality, and the magnetic polarization of the higher field became the determining factor for modern clinical MRI systems. The engineering of MRI systems has improved significantly because of homogeneous magnet design, fast shielded gradient systems that minimize eddy currents, phased-array receiver coils, and advanced image reconstructions that use abundant and inexpensive computational power. Commercial low-field-strength MRI systems are relegated to niche applications and have not benefited from these advances. To our knowledge, our study is the first to combine a low field strength with contemporary high-performance hardware.

This technology could be important for some clinical applications. The lack of safe metal devices has limited MRI guidance of cardiovascular procedures (28). We anticipate that low-field-strength MRI will enable MRI-guided procedures that use a subset of devices from the traditional catheterization environment.

Superior image quality of the lung, near the cranial sinuses, and near the intestines may allow diagnostic examinations on these neglected anatomic regions. This image quality is dependent on field homogeneity from state-of-the-art magnet design. Additionally, in the lung, oxygen can be used as an inexpensive, readily available, and physiologically relevant contrast agent that performs better at lower field (29).

The SNR-efficient long readout strategies explored here may be useful at this field strength. We expect image quality of these methods to be higher at 0.55 T versus 1.5 T because of reduced distortions and blurring. Advanced image reconstructions offer a complementary strategy to recover signal (2).

The use of a low-field-strength system has several critical workflow benefits. For example, the magnetohydrodynamic effect that causes electrocardiogram distortion is reduced at low fields, meaning that patient monitoring is improved. The patient care environment is more comfortable because of reduced acoustic noise and reduced vestibular upset at lower fields (30,31). Low-field MRI is also inherently cost-effective because of the reduced magnet, radiofrequency amplifier, and siting costs (1), which could have important implications for access to care and technology dissemination. In addition to the applications described here, a high-performance low-field-strength system could also enable other imaging techniques limited by artifacts or specific absorption rate restrictions at higher fields and those that exploit the favorable relaxation properties.

There were also some limitations to our study. The receiver coils used in this study were retuned from 1.5 T and therefore were not optimized for low field strength and resulted in image shading. Larger coil elements were chosen to maintain sample-dominated noise; however, this sacrifices parallel imaging performance. Only a small subset of routine clinical imaging protocols was attempted in this initial study and future studies will assess the diagnostic capabilities of this high-performance low-field-strength system.

By using a high-performance lowfield-strength MRI system, there are opportunities for the development of new techniques for invasive MRI-guided procedures, to design acquisition and reconstruction strategies, and for contrast agent development and hardware design. This technology warrants further investigation in the context of clinical MRI.

Acknowledgments: We acknowledge the contributions of William Schenke, BA, Annette Stine, BSN, RN, and Laurie Grant, CRNP, MS, for patient care in the catheterization laboratory. We also thank Margaret (Peg) Lowery, RN, Jennifer Henry, RN, and Sujata Shanbhag, MD, MPH, for volunteer recruitment and clinical assistance during diagnostic imaging. Lanelle Edwards, BS, is acknowledged for her assistance in preparation of contrast agent phantoms, and Olga Vasalatiy, PhD, and Ana Opina, PhD, for provision of the gadolinium-dendrimers.

Author contributions: Guarantors of integrity of entire study, A.E.C.W., R.S.B.; study concepts/study design or data acquisition or data analysis/interpretation, all authors; manuscript drafting or manuscript revision for important intellectual content, all authors; approval of final version of submitted manuscript, all authors; agrees to ensure any questions related to the work are appropriately resolved, all authors; literature research, A.E.C.W., I.B., M.S.H., A.A.M., A.P.K., R.S.B.; clinical studies, A.E.C.W., T.R., W.P.B., C.M., J.M., A.A.M., E.C.J., M.Y.C., R.J.L., D.R.M.; experimental studies, A.E.C.W., R.R., M.C.R., I.B., B.B., D.A.H., W.P.B., D.R.M., C.M., H.X., P.K., M.Y.C., R.J.L., R.S.B., A.P.K., R.S., D.G., W.M., H.B.; statistical analysis, A.E.C.W., I.B.; and manuscript editing, A.E.C.W., I.B., B.B., D.A.H., M.S.H., W.P.B., D.R.M., D.G., R.S., H.B., H.X., A.A.M., E.C.J., A.P.K., P.K., M.Y.C., R.J.L., R.S.B.

Disclosures of Conflicts of Interest: A.E.C.W. Activities related to the present article: author disclosed that the National Heart Lung and Blood Institute has a collaborative research and development agreement on MRI that includes the work described in this study. Activities not related to the present article: disclosed no relevant relationships. Other relationships: disclosed no relevant relationships. **R.R.** disclosed no relevant relationships. **M.C.R.** disclosed no relevant relationships. **I.B.** disclosed no relevant relationships. **B.B.** disclosed no relevant relationships. **D.A.H.** disclosed no relevant relationships. **M.S.H.** disclosed no relevant relationships. **T.R.** Activities related to the present article: disclosed no relevant relationships. Activities not related to the present article: disclosed money paid to author for consultancy from Medtronic; disclosed that author receives money from Edwards Lifesciences for consultancy. Other relationships: disclosed no relevant relationships. **W.P.B.** disclosed no relevant relationships. **D.R.M.** disclosed no relevant relationships. **C.M.** disclosed no relevant relationships. **D.G.** Activities related to the present article: disclosed no relevant relationships. Activities not related to the present article: disclosed money paid to author from Siemens Healthcare for employment and patents. Other relationships: disclosed no relevant relationships. **R.S.** Activities related to the present article: disclosed no relevant relationships. Activities not related to the present article: disclosed employment from Siemens Healthcare. Other relationships: disclosed no relevant relationships. **W.M.** Activities related to the present article: disclosed no relevant relationships. Activities not related to the present article: disclosed employment from Siemens Healthcare. Other relationships: disclosed no relevant relationships. **H.B.** Activities related to the present article: disclosed no relevant relationships. Activities not related to the present article: disclosed employment from Siemens Healthcare. Other relationships: disclosed no relevant relationships. **H.X.** disclosed no relevant relationships. **J.M.** disclosed no relevant relationships. **A.A.M.** disclosed no relevant relationships. **E.C.J.** disclosed no relevant relationships. **A.P.K.** disclosed no relevant relationships. **P.K.** disclosed no relevant relationships. **M.Y.C.** disclosed no relevant relationships. **R.J.L.** Activities related to the present article: author disclosed that the National Heart Lung and Blood Institute has a collaborative research and development agreement on MRI that includes the work described in this study. Activities not related to the present article: disclosed no relevant relationships. Other relationships: disclosed no relevant relationships. **R.S.B.** Activities related to the present article: author disclosed that the National Heart Lung and Blood Institute has a collaborative research and development agreement on MRI that includes the work described in this study. Activities not related to the present article: disclosed no relevant relationships. Other relationships: disclosed no relevant relationships.

References

1. Marques JP, Simonis FFJ, Webb AG. Low-field MRI: An MR physics perspective. J Magn Reson Imaging 2019;49(6):1528–1542.

2. Simonetti OP, Ahmad R. Low-Field Cardiac Magnetic Resonance Imaging: A Compelling Case for Cardiac Magnetic Resonance's Future. Circ Cardiovasc Imaging 2017; 10(6):e005446.
3. Rashid S, Han F, Gao Y, et al. Cardiac balanced steady-state free precession MRI at 0.35 T: a comparison study with 1.5 T. Quant Imaging Med Surg 2018;8(7):627–636.
4. Rogers T, Lederman RJ. Interventional CMR: Clinical applications and future directions. Curr Cardiol Rep 2015;17(5):31.
5. Konings MK, Bartels LW, Smits HF, Bakker CJ. Heating around intravascular guidewires by resonating RF waves. J Magn Reson Imaging 2000;12(1):79–85.
6. ASTM International. F2182-09 Standard Test Method for Measurement of Radio Frequency Induced Heating On or Near Passive Implants During Magnetic Resonance Imaging. West Conshohocken, Pa: ASTM International, 2009.
7. Campbell-Washburn AE, Rogers T, Stine AM, et al. Right heart catheterization using metallic guidewires and low SAR cardiovascular magnetic resonance fluoroscopy at 1.5 Tesla: first in human experience. J Cardiovasc Magn Reson 2018;20(1):41.
8. Velasco Forte MN, Pushparajah K, Schaeffter T, et al. Improved passive catheter tracking with positive contrast for CMR-guided cardiac catheterization using partial saturation (pSAT). J Cardiovasc Magn Reson 2017;19(1):60.
9. Johnson SR, Taveira-DaSilva AM, Moss J. Lymphangioleiomyomatosis. Clin Chest Med 2016;37(3):389–403.
10. Edelman RR, Hatabu H, Tadamura E, Li W, Prasad PV. Noninvasive assessment of regional ventilation in the human lung using oxygen-enhanced magnetic resonance imaging. Nat Med 1996;2(11):1236–1239.
11. Dietrich O, Gaass T, Reiser MF. T1 relaxation time constants, influence of oxygen, and the oxygen transfer function of the human lung at 1.5T-A meta-analysis. Eur J Radiol 2017;86:252–260.
12. Bulte D, Chiarelli P, Wise R, Jezzard P. Measurement of cerebral blood volume in humans using hyperoxic MRI contrast. J Magn Reson Imaging 2007;26(4):894–899.
13. Lingala SG, Sutton BP, Miquel ME, Nayak KS. Recommendations for real-time speech MRI. J Magn Reson Imaging 2016;43(1):28–44.
14. Lingala SG, Zhu Y, Kim YC, Toutios A, Narayanan S, Nayak KS. A fast and flexible MRI system for the study of dynamic vocal tract shaping. Magn Reson Med 2017;77(1):112–125.
15. Feng L, Grimm R, Block KT, et al. Golden-angle radial sparse parallel MRI: combination of compressed sensing, parallel imaging, and golden-angle radial sampling for fast and flexible dynamic volumetric MRI. Magn Reson Med 2014;72(3):707–717.
16. Nayak KS, Hargreaves BA, Hu BS, Nishimura DG, Pauly JM, Meyer CH. Spiral balanced steady-state free precession cardiac imaging. Magn Reson Med 2005;53(6): 1468–1473.
17. Li Z, Hu HH, Miller JH, et al. A Spiral Spin-Echo MR Imaging Technique for Improved Flow Artifact Suppression in T1-Weighted Postcontrast Brain Imaging: A Comparison with Cartesian Turbo Spin-Echo. AJNR Am J Neuroradiol 2016;37(4):642–647.
18. Campbell-Washburn AE, Xue H, Lederman RJ, Faranesh AZ, Hansen MS. Real-time distortion correction of spiral and echo planar images using the gradient system impulse response function. Magn Reson Med 2016;75(6):2278–2285.
19. Macovski A. Noise in MRI. Magn Reson Med 1996;36(3):494–497.
20. Robson PM, Grant AK, Madhuranthakam AJ, Lattanzi R, Sodickson DK, McKenzie CA. Comprehensive quantification of signal-to-noise ratio and g-factor for image-based and k-space-based parallel imaging reconstructions. Magn Reson Med 2008;60(4): 895–907.
21. Lim Y, Lingala SG, Narayanan SS, Nayak KS. Dynamic off-resonance correction for spiral real-time MRI of speech. Magn Reson Med 2019;81(1):234–246.
22. Rohrer M, Bauer H, Mintorovitch J, Requardt M, Weinmann HJ. Comparison of magnetic properties of MRI contrast media solutions at different magnetic field strengths. Invest Radiol 2005;40(11):715–724.
23. Vasanawala SS, Nguyen KL, Hope MD, et al. Safety and technique of ferumoxytol administration for MRI. Magn Reson Med 2016;75(5):2107–2111.
24. Finn JP, Nguyen KL, Han F, et al. Cardiovascular MRI with ferumoxytol. Clin Radiol 2016;71(8):796–806.
25. Richardson OC, Bane O, Scott ML, et al. Gadofosveset-based biomarker of tissue albumin concentration: Technical validation in vitro and feasibility in vivo. Magn Reson Med 2015;73(1):244–253.
26. Opina AC, Wong KJ, Griffiths GL, et al. Preparation and long-term biodistribution studies of a PAMAM dendrimer G5-Gd-BnDOTA conjugate for lymphatic imaging. Nanomedicine (Lond) 2015;10(9):1423–1437.
27. Longmire MR, Ogawa M, Choyke PL, Kobayashi H. Dendrimers as high relaxivity MR contrast agents. Wiley Interdiscip Rev Nanomed Nanobiotechnol 2014; 6(2):155–162.
28. Ratnayaka K, Faranesh AZ, Guttman MA, Kocaturk O, Saikus CE, Lederman RJ. Interventional cardiovascular magnetic resonance: still tantalizing. J Cardiovasc Magn Reson 2008;10(1):62.
29. Mirhej ME. Proton Spin Relaxation By Paramagnetic Molecular Oxygen. Can J Chem 1965;43(5):1130–1138.
30. van Osch MJP, Webb AG. Safety of Ultra-High Field MRI: What are the Specific Risks? Curr Radiol Rep 2014;2(8):61.
31. Price DL, De Wilde JP, Papadaki AM, Curran JS, Kitney RI. Investigation of acoustic noise on 15 MRI scanners from 0.2 T to 3 T. J Magn Reson Imaging 2001;13(2): 288–293.
32. Messroghli DR, Radjenovic A, Kozerke S, Higgins DM, Sivananthan MU, Ridgway JP. Modified Look-Locker inversion recovery (MOLLI) for high-resolution T1 mapping of the heart. Magn Reson Med 2004;52(1):141–146.